Cracking-controlled slurry coating of mosaic electrode for flexible and high-performance lithium-sulfur battery

*Yufeng Luo, Lei Wang, Zhenyao Wei, Qiyao Huang, Zijian Zheng**

Dr.Y. Luo, Dr. L. Wang, Z. Wei, Prof. Q. Huang, Prof. Z. J. Zheng

Laboratory for Advanced Interfacial Materials and Devices, Institute of Textiles and Clothing, The Hong Kong Polytechnic University, Hong Kong SAR, China.

Dr.Y. Luo, Prof. Z. Zheng

Research Institute for Intelligent Wearable Systems, The Hong Kong Polytechnic University, Hong Kong SAR, China.

Prof. Z. Zheng

Research Institute for Smart Energy, The Hong Kong Polytechnic University, Hong Kong SAR, China.

E-mail: tczzheng@polyu.edu.hk

Keywords: mosaic structure, crack, slurry, lithium-sulfur battery, flexible battery

Abstract: Future wearable applications require high-energy-density flexible batteries. Lithium-sulfur (Li-S) battery is a competitive candidate because of the large abundance and high theoretical specific capacity of S. The fabrication of high-mass-loading and high-performance S cathode is a critical step to achieve high energy density of the battery. However, those high-performance S cathodes reported to date require complicated and time-consuming fabrication processes that are difficult to scale up. On the other hand, thick S cathodes fabricated with conventional high-speed slurry coating method show poor flexibility and electrochemical performance due to the unpredictable cracking of the S electrode during bending and

charge/discharge. Herein, we develop a high-speed cracking-controlled slurry coating method, which spontaneously generates a mosaic-like regular cracks of the S cathode. When the S slurry is coated and dried on an interlacing metallic fabric, mosaic-like cracks following the pattern of the interlaces form due to the difference of wetting on the fabric surface. These pre-formed cracks provide vertical channels to facilitate the rapid diffusion of electrolyte, adequate space to accommodate the large volume expansion during cycling, and strain-releasing sS1tructure to achieve high flexibility. As a result, thick Mosaic-S cathodes (9 mAh cm^{-2}) provide outstanding energy density (560 Wh kg^{-1}), long cycle life over 500 cycles, and outstanding flexibility under dynamic bending. Importantly, the fabrication throughput of the cracking-controlled method is similar to that of the industrial slurry coating process. This work paves the way for scalable fabrication of high-performance S cathodes in the near future.

1. Introduction

Lithium-sulfur (Li-S) battery has received much attention in the past decade because of the high energy density, low cost, natural abundance, and easy recycling of elemental sulfur.[1-5] These advantages are particularly suitable for high-performance flexible and wearable applications, where low-profile flexible batteries are essential to seamlessly integrate into the electronic parts to provide omnidirectionally bendable devices and systems.[6-8] In recent years, a tremendous amount of effort has been focused on constructing flexible S cathodes on current collectors made with carbon materials, such as carbon nanofiber, carbon nanotube, and graphene.[9-12] Benefiting from the outstanding mechanical flexibility and electrical conductivity of carbon-based current collectors, several high-performance flexible Li-S batteries have been reported.[13-31]

Nevertheless, the fabrication of these flexible S electrodes required complicated and time-consuming processes. For example, the construction of carbon-based macroscopic current collectors typically required the use of chemical vapor deposition, vacuum filtration, free drying,

or a combination of those.[13-17] Additional functionalization of the carbon-based current collectors were realized through chemical doping of heteroatoms, hydrothermal reaction, grafting of S-affinity or S-containing species,[18-24] following complex S infusion procedure. [25-29] Although these processes can significantly improve the cycling stability of the flexible S electrodes, they are difficult to scale up and unlikely to be implemented in industrial roll-to-roll manufacture.

In the battery industry, slurry coating is a standard and high-throughput method for manufacturing battery electrodes.[32,33] In the slurry coating process, a liquid slurry containing solvent, active materials, conducting agents, binders, and other additives is coated onto the current collector, followed by drying to form a solid composite film. Although there have been reports trying to use slurry coating to prepare S cathodes, those electrodes showed poor performance because of the following reasons. 1) The electrodes prepared by the conventional slurry coating method are dense and show high tortuosity. This structure not only leads to difficulty in wetting the entire electrode with liquid electrolyte, but also hampers ionic transportation, especially at high rates.[34-36] 2) The significant volume expansion and contraction of S particles during the dicharge/charge processes result in uncontrolled cracking of the electrode, which significantly degrades the electrochemical performance.[37,38] The disadvantages of high tortuosity and high volume change discussed above are more prominent when the thickness of the electrode increases.[39] 3) Bending those thick S cathodes will generate uncontrolled cracks and even delamination of the electrodes, which rapidly deteriorates the electrochemical performance of the battery.[40] Despite numerous recent attempts on developing new binders or applying S-stabilizing materials, it is still very challenging to prepare flexible and high-performance S cathodes using a simple slurry coating method.

Herein, we report a simple cracking-controlled slurry coating method to generate mosaic-like cracks on S (Mosaic-S) cathodes, which provides pre-defined microstructures benefiting the mechanical flexibility and electrochemical stability of the S cathodes. The cracking-

controlled mechanism is based on the difference of surface tension on the woven structure of conductive fabrics. When the liquid slurry is coated on top, it is preferentially pinned on the protruded interlacing positions of the weft and warp yarns of the conductive fabric due to the higher surface tension.[41-43] As such, microcracks will form between neighboring interlacing positions during the subsequent drying process, and a mosaic-like cracking structure following the fabric template is generated at a suitable viscosity of the slurry (Fig. 1a). These pre-formed microcracks provide free space to accommodate the volume expansion of the active materials, facilitate the deep penetration of the electrolyte and improve the ionic transfer, and define a stable breakage pattern of the electrode during bending. Therefore, the Mosaic-S possesses stable electrode morphology, strong adhesion, high rate, and long lifespan during repeating bending and electrochemical cycling tests. By using the Mosaic-S, we demonstrate a Li-S battery of high areal capacity over 8.6 mAh cm^{-2} and high energy density of 550 Wh kg^{-1} (480 Wh L^{-1}). Incorporated with a flexible Li metal anode, we demonstrate a highly flexible Li-S battery that can be bent in arbitrary directions and shows negligible shift of charge-discharge voltage profiles during 7800 cycles of continuous bending at a very small bending radius of 5 mm.

Importantly, the cracking-controlled method is compatible with the industrial slurry coating process of battery manufacturing, and does not require any additional pre-treatment or post-treatment steps. Therefore, it addresses the challenge of high-throughput fabrication of thick, stable, and flexible S cathodes. Moreover, since the cracking-controlled mechanism is based on the surface wetting process, this method can be easily applied to a wide range of electrode materials, offering a simple and cost-effective strategy to manufacture high-performance flexible batteries.

2. Results and Discussion

As a proof of concept, Ni-coated carbon cloth (NiCC) was used as the flexible current collector (Fig. 1b). The Ni coating increased the conductivity of the CC and facilitated the redox reaction of polysulfide.[31] The S-containing slurry in N-methylpyrrolidone (NMP) was coated on the NiCC, and the slurry was rapidly absorbed onto the surface of NiCC and infiltrated into 3D gaps between the fibers and yarns because of the capillary effect. The sample was then dried by heating to evaporate the NMP. Unlike conventional planar Al foils where liquid slurry often dries out uniformly to form a flat electrode film (Fig. S1, denoted here as S-Al), the woven structure provides a significant difference of the wettability: liquid prefers to pin on the interlacing positions where the warp yarns go across the weft. Therefore, during the drying process, the S electrode gradually aggregated on the interlacing areas of NiCC, which generated lateral forces to break the liquid layer on the connecting areas in between the interlaces (optical images inset in Fig. 1a).

We found that when the viscosity of the slurry was well controlled by changing the ratio between the NMP and the other components (Fig. S2), regular cracks were formed in between the interlaces after the electrode was fully dried. At this point, a Mosaic-S cathode following the pattern of the woven structure was fabricated (Fig. 1c, mass ratio of 7). From the cross-sectional SEM image of the Mosaic-S cathode, the pre-formed cracks almost penetrated the entire S layer. We also found that when the viscosity was too low or too high, random cracks with different cracking densities formed, which has been explained as a result of uneven internal stress during the drying process (Fig. 1d, 1e, and S3) [44,45]. Note that there were two typical morphologies of the S cathodes with random cracks. The first type showed a more continuous S layer with short surface cracks (denoted here as Microfissure-S, mass ratio of 7.5, Fig. 1c), while the other exhibited a percalative morphology with a much higher density of cracks (denoted here as Takyr-S, mass ratio of 8.5, Fig. 1d). Nevertheless, none of these cracks followed the pattern of the woven structure of the NiCC, and most of these cracks occur on the surface but do not extend to the depth of the S layer (Fig. S4).

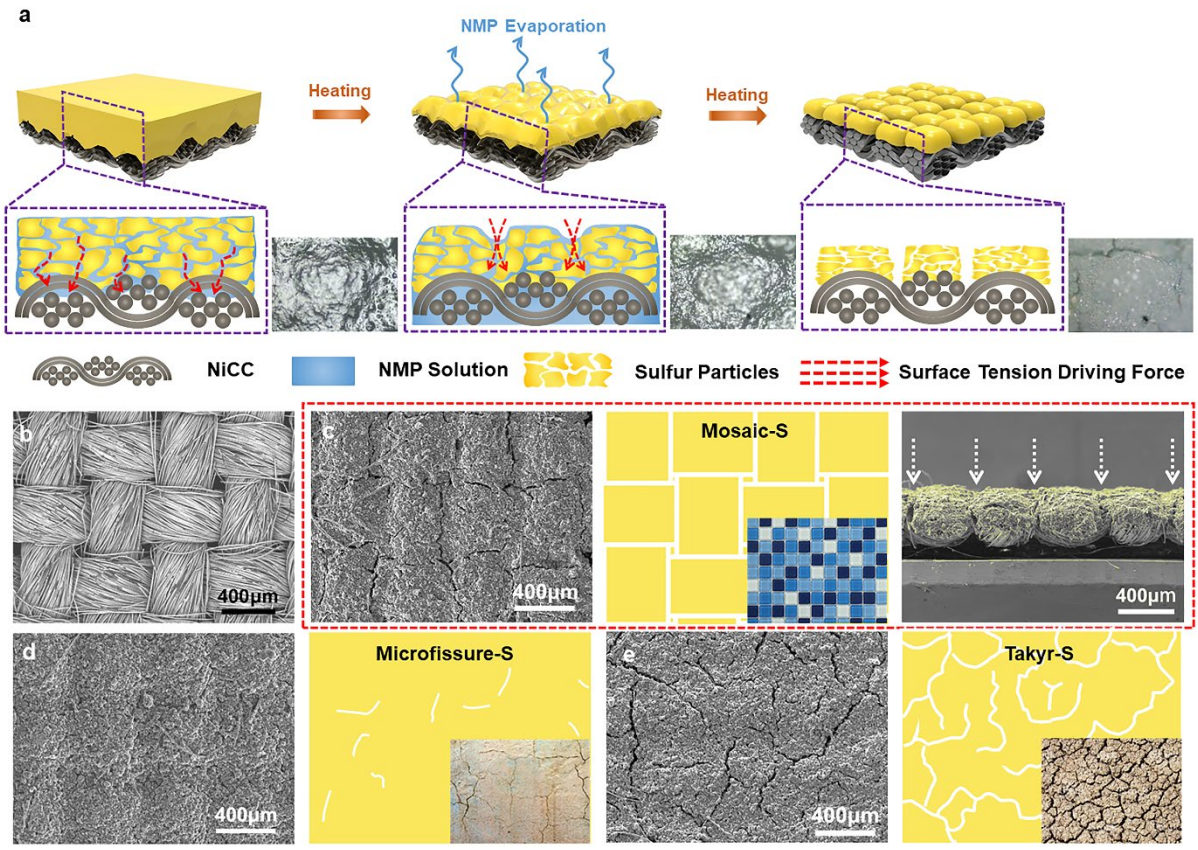

Figure 1. Cracking-controlled slurry coating of S cathodes. a) Schematics of the cracking-controlled slurry coating process of S cathodes on Ni-coated carbon cloth (NiCC). b) SEM image of NiCC. SEM and schematics of the structure of c) Mosaic-S, d) Microfissure-S (mass ratio of 7.5), and e) Takyr-S cathodes (mass ratio of 8.5).

Importantly, the mosaic-like cracks served as vertical channels to increase the ionic transfer rates, which effectively decreased the tortuosity of the S electrode. To quantify the tortuosity, we assembled an electrochemical test cell following a reported method,[46] where the S electrode was sandwiched between one pair of Li foils and spacers (schematic in Fig. 2a). We applied a constant current density of 10^{-5} A to the cell for 2 h to generate a concentration gradient of Li^+. The current was then cut off, where the test cell underwent a relaxation period (t) until its potential (U) approached equilibrium (Fig. 2a). During this period, Li^+ flux passed through the

entire S cathode, and the speed of diffusion, diffusivity (D), was used to determine the tortuosity (τ) of the S electrode. D is proportional to the slope of the linear regime of the $\ln|U(t) - U(t = \infty)|$ vs. t plot (Fig. 2b), and it could be expressed using equation (1):[47,48]

$$t^{\delta} = \frac{L^2}{\pi^2 D} \quad (1)$$

where L is the electrode thickness, and t^{δ} is the characteristic value representing the relaxation time of the depolarization process.

As such, τ could be obtained using equation (2): [49,50]

$$\tau = \epsilon \frac{D_0}{D} \quad (2)$$

where ε is the electrode porosity, and D_0 is the intrinsic diffusivity of the Li^+ without the S electrode (Fig. S5).

Table 1 summarizes the test results. τ of Mosaic-S, Microfissure-S, and Takyr-S electrodes were 1.04, 2.23 and 2.75, respectively. The low tortuosity of Mosaic-S is ascribed to the deep penetration of the pre-form cracks through the entire S electrode (Fig. 2c). In contrast, random cracks only formed on the surface layer of Microfissure-S and Takyr-S, so that the ionic diffusions are significantly hindered (Fig. 2d and 2e).

Cyclic voltammetry (CV) and electrochemical impedance spectroscopy (EIS) tests evidenced the efficient ionic diffusion of the low-tortuosity Mosaic-S electrode. There are two cathodic peaks corresponding to the reductions of S_8 to polysulfides and polysulfides to Li_2S_2/Li_2S, respectively (Fig. 2f). The two anodic peaks correspond to the oxidation reactions of the reverse transformation. Mosaic-S and Takyr-S cathodes showed a distinctive shift in the redox peaks compared to the Microfissure-S cathode, and the Mosaic-S exhibited the highest current response. Besides, after fitting the obtained Nyquist plots according to the equivalent circuit model (inset in Fig. 2g), Mosaic-S and Takyr-S cathodes showed much smaller charge-transfer resistance (R_{ct}) than the Microfissure-S cathode because of the existence of the cracks (Table S1). There is another depressed semicircle shown in the high-frequency region,

simulating the process of electron from the current collector to the reaction sites (interphase contact resistance, R_{int}).[51] "The highest density of cracks in the Takyr-S resulted in the largest R_{int} value among the three kinds of S electrodes." All these results demonstrate that the mosaic-like microstructure can benefit the redox reaction of the sulfur species in both aspects of electron transmission and Li^+ transformation.

As a consequence of the improved ionic transfer, the Mosaic-S cathode showed a superior specific capacity, especially at high rates, to Takyr-S and Microfissure-S. The Mosaic-S cathode delivered reversible specific capacities of 1166.1, 1085.2, 931.3, 717.9, and 364.4 mAh g^{-1} when charged and discharged at 0.1, 0.2, 0.5, 1, and 2 C, respectively (Fig. 2h, and S6). In comparison, the capacities of Takyr-S and Microfissure-S were much lower at the same testing conditions. For example, at 1C, the capacities of Microfissure-S and Takyr-S were 602.3 and 206.6 mAh g^{-1} only.

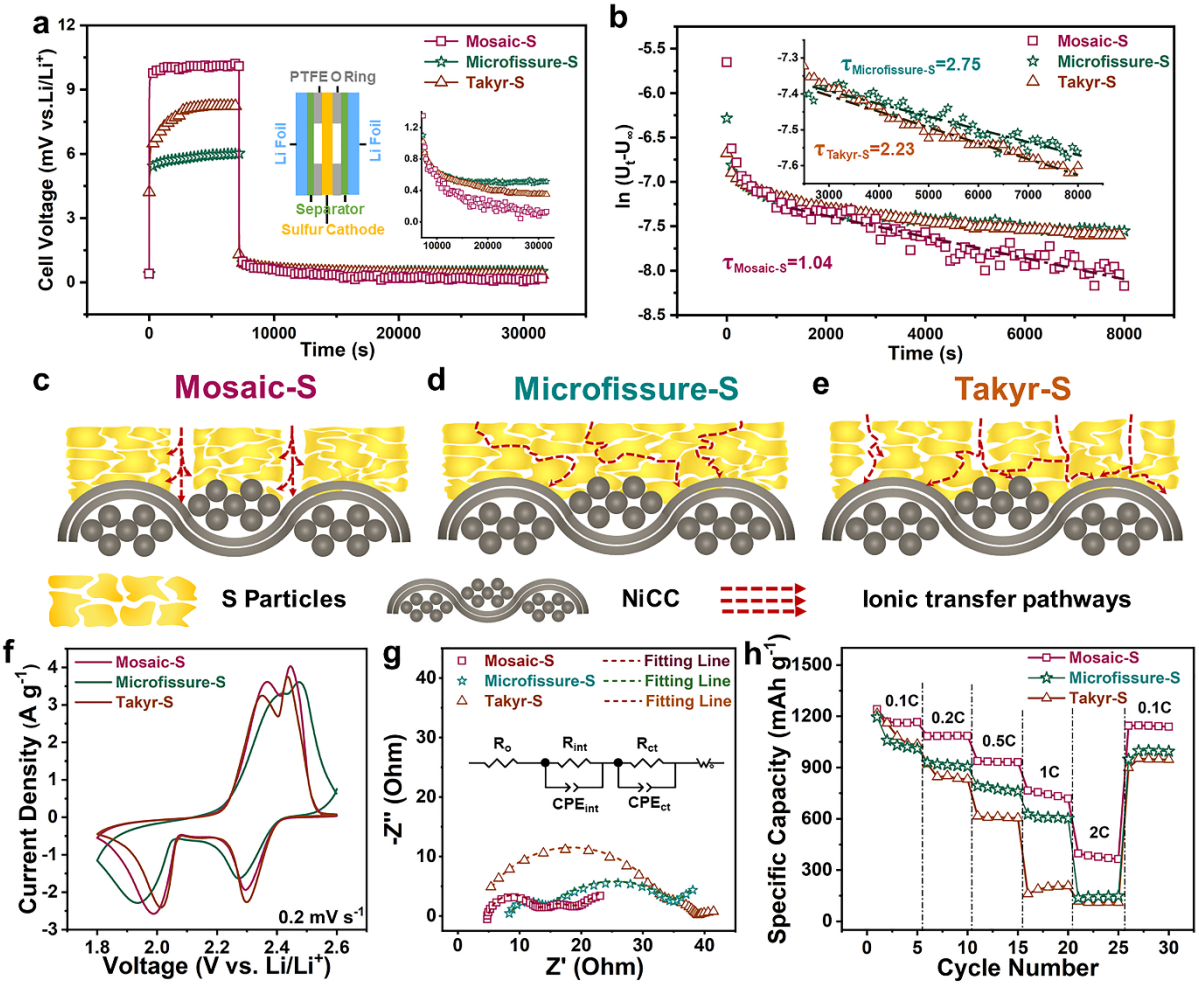

Figure 2. Low Tortuosity. a, b) Polarization-depolarization plots of the asymmetric cell and the corresponding $\ln|U(t) - U(t = \infty)|$ versus t plots during the depolarization period of the Microfissure-S, Takyr-S, and Mosaic-S cathodes, the dash-dotted line was the fitting data in the linear regime. c-e) Schematics illustrating the ion transfer pathways in the Mosaic-S, Microfissure-S, and Takyr-S cathodes. f-h) CV curves, Nyquist plots, and rate performance of the Pristine-S-Al, Microfissure-S, Takyr-S, and Mosaic-S cathodes.

Table 1. Effective diffusivities, porosities, and calculated tortuosities of the sulfur cathodes.

	$\ln\left\|U(t)-U(t=\infty)\right\|$	Slope	L (μm)	Diffusivity ($cm^2\ s^{-1}$)	ε (%)	τ
Mosaic-S	y=-1.17×10^{-4}x-7.15	-1.17×10^{-4}	350	1.79×10^{-8}	58.66	1.04
Microfissure-S	y=-4.47×10^{-5}x-7.23	-4.47×10^{-5}	350	6.84×10^{-9}	56.83	2.75
Takyr-S	y=-5.43×10^{-5}x-7.21	-5.43×10^{-5}	350	8.31×10^{-9}	59.37	2.23

More importantly, the Mosaic-S showed outstanding structure stability upon charge/discharge, which significantly enhanced the cycling stability. As a proof of concept, we cycled the three electrodes at a low rate of 0.2 C at a mass loading of 2.6 mg cm^{-2} (Fig. 3a). The initial capacities of the three electrodes at 0.05 C at the first cycle were similar, being 1250 mAh g^{-1}. However, after just five cycles at 0.1 C, the capacities of Microfissure-S and Takyr-S dropped rapidly to 1039, and 904 mAh g^{-1}, respectively. The capacity deterioration can be associated with the structural instability of electrode during cycling. We found the formation of a large number of random cracks on both Microfissure-S and Takyr-S electrodes (Fig. 3b and 3c), in addition to their existing cracks, after the short cycles. These additional cracks mainly resulted from the volume change of the S electrode during cycling. In contrast, the capacity of Mosaic-S only decreased slightly to 1075 mAh g^{-1}. The microstructure of the Mosaic-S did not show obvious change before and after cycling (Fig. 3d). It is most likely to be ascribed to the regular deep cracks in Mosaic-S, which provided adequate space to accommodate the volumetric variation to avoid the generation of additional irregular cracks. We then continued to cycle these cells to 50 cycles at 0.2 C. The Mosaic-S did not show obvious capacity decade, while the capacities of both Microfissure-S and Takyr-S electrodes continued to decrease to 885 and 664 mAh g^{-1}. Benefiting from the excellent structural stability and low tortuosity, the Mosaic-S cathode exhibited a long lifespan. After 500 cycles at 0.5 and 1 C, the capacities only

dropped by 603 and 547 mAh g^{-1}, corresponding to low capacity attenuation rates of 0.056 % and 0.047 % per cycle, respectively (Fig. 3e).

We also tested Mosaic-S electrodes with increasing mass loading of S to 3.0, 4.8, and 8.6 mg cm^{-2}. (Fig. 3f). For the cells with 3.0 and 4.8 mg cm^{-2} of S, the electrochemical characteristics were similar to that of the one with 2.6 mg cm^{-2}. The areal capacities were 3.75 and 5.70 mAh cm^{-2} respectively (~ 1200 mAh g^{-1}) at the first cycle, and then decreased to 3.13 (97.5 %) and 3.91 (85.2 %) mAh cm^{-2} 50 cycles. The Mosaic-S electrode with an 8.6 mg cm^{-2} mass loading, benefiting from the vertical crack channels (Fig. S7), can still show a high areal capacity of 8.64 mAh cm^{-2} (~ 1004 mAh g^{-1}) at the first cycle, and then decreased to 5.19 mAh cm^{-2} after 50 cycles, corresponding to a high specific energy density of 560 Wh kg^{-1} (260 Wh kg^{-1} including the electrolyte, Table S2). As a comparison, commercial S electrodes coated on Al foils only displayed a low initial capacity of 0.60 mAh cm^{-2} at 0.2 C. Notably, the achieved high loading performance is also compared with the recent state-of-the-art S cathodes based on carbon clothes when taking the critical parameters of the mass loading, cycle number, current density, and capacity retention into account in Table S4. The Mosaic-S cathode shows an advanced performance with high sulfur loading fabricated by such a simple fabrication method.

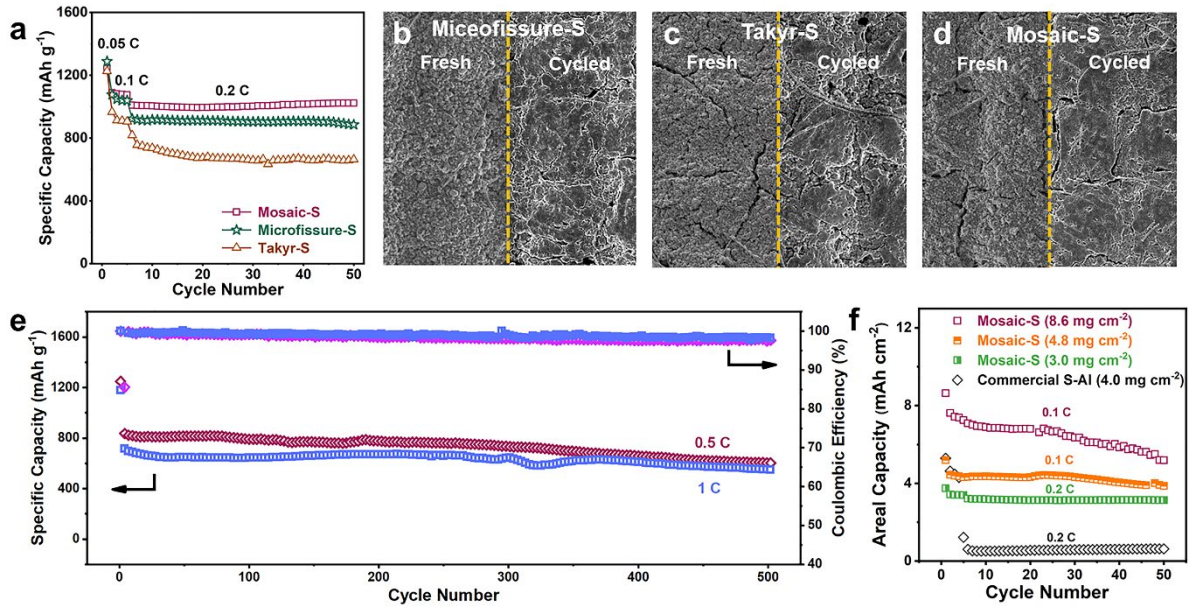

Figure 3. Cycling Performance. a) Cyclic performance of the Microfissure-S, Takyr-S, and Mosaic-S cathodes at 0.2 C. b-d) SEM images of the top surface of the fresh and cycled Microfissure-S, Takyr-S, and Mosaic-S cathodes. e) Cyclic performance of the Mosaic-S cathode at current densities of 0.5 C and 1 C, respectively. f) Cyclic performance of the Mosaic-S cathode with a mass loading of 8.6, 4.8 and 3 mg cm^{-2}, respectively.

Apart from enhancing the electrochemical performance, the mosaic structures also enable high mechanical flexibility of the S electrode. Three sets of electrodes including Mosaic-S, Microfissure-S, and S-Al were evaluated for demonstration. Because of the larger interfacial area between the S electrodes and the 3D fabrics than the planar Al, the shear strength of the Mosaic-S and Microfissure-S were 0.15 and 0.11 MPa, nearly 4.8 and 3.6 times higher than that of S-Al (Fig. 4a). Therefore, when these electrodes were bent, fracture and delamination readily occurred on S-Al (Fig. 4b), while the Mosaic-S and Microfissure-S still adhered on the fabric (Fig. 4c and 4d). Observing from the top surface of the Mosaic-S cathode bent at a radius of 1mm (Fig. S8), we did not find obvious cracks on the surface of each S block, indicating the integrity of the Mosaic-S cathode under the bending state.

Notably, because the pre-formed regular cracks in Mosaic-S were deep enough, the structure of Mosaic-S was highly stable when the electrode was bent (Fig. 4e). The sheet resistance of Mosaic-S was 0.57 Ω sq^{-1}, and it only increased by 25% after 10,000 cycles of continuous bending at a radius of 5 mm. On the other hand, because the random cracks in Microfissure-S mostly stayed on the surface, we observed not only crack propagation, but also formation of many new cracks when it was bent (inset in Fig. 4e). As a consequence, the sheet resistance of Microfissure-S increased by more than two folds. The R_{ct} of the Microfissure-S cathode is also increased five folds, while the Mosaic-S cathode was almost unchanged after 10000 times bending (Fig. S9, and Table S3).

We fabricated high-performance flexible Li-S battery by paring the Mosaic-S cathode with a flexile Li metal anode (Fig. 4f). The Li metal anode was fabricated using a literature method and the morphology is shown in Fig. S10.[31] Compared with Li Foil, the symmetric cell of the electrodeposited Li anode based on the NiCC exhibited much better cyclic performance. The mass loading of the Mosaic-S cathode was ~3 mg cm^{-2} and the N/P ratio was controlled to be 1.66:1. As shown in Fig. 4g, the open-circuit voltage (OCV) of the cell was 2.67 V, and it was insensitive to bending from 0° to 180°. The OCV showed subtle fluctuations of less than 60 mV during 2,000 bending cycles, in contrast to the rapid OCV drop of the cell made with S-Al. We also charged and discharged the flexile cell while it was dynamically bent (Fig. 4h). The Mosaic-S-based Li-S cell exhibited zero shift of the voltage profiles during the 7800 bending cycles, while the S-Al-based cell failed after 300 cycles. After the dynamic bending test, the Mosaic-S cell could still stably cycle at a higher current of 2 mA. The flexible Li-S cells could stability power a light-emitting diodes (LED) array consisting of thirty yellow LEDs while they were bent or folded at different configurations shown in Fig.4i. The cyclic performance of the pouch cell with a 6 mg cm^{-2} mass loading was also performed under a condition of 6.7 μL mg_s^{-1} (Fig. S11). The cell delivered an initial areal capacity of 6.71 mAh cm^{-2} (1117.48 mAh g^{-1}), corresponding to a specific energy density of 621 Wh kg^{-1} (214 Wh kg^{-1} including the electrolyte). The capacity decreased to 3.74 mAh cm^{-2} (623.75 mAh g^{-1}) after 30 cycles at a current of 2 mA (0.033 C).

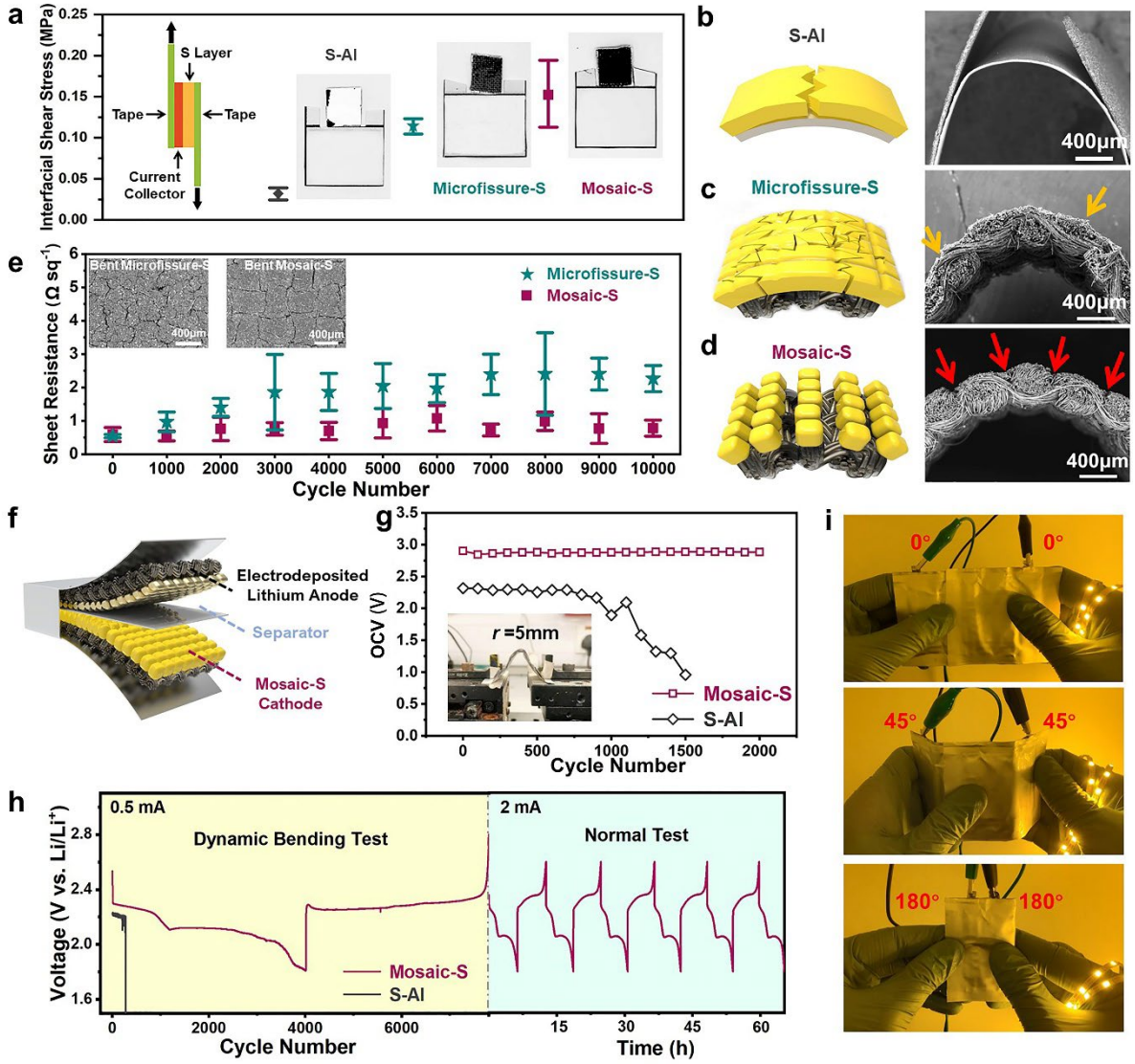

Figure 4. Electrochemical Performance. a) Setup for the single-lap shear tests, interfacial test results of the S-Al, Microfissure-S, and Mosaic-S cathodes, and their corresponding fracture surfaces. b-d) Schematics and cross-section SEM images of S-Al, Microfissure-S, and Mosaic-S cathodes. e) The sheet resistance of the Microfissure-S and Mosaic-S cathodes in the 10000 bending times, and their corresponding SEM images after bending. f) Schematics of the full cell of Mosaic-S cathode coupled with an electrodeposited lithium anode. g) OCV stability of the assembled full cells with Mosaic-S and S-Al cathodes during 2000 bending times at a radius of 5 mm. h) Voltage profiles of the assembled full cells under an operando bending tests at a radius of 5 mm with a bending rate of 1mm s^{-1}. i) The assembled series full cells in various folded states and their LED illuminating test.

To further demonstrate the versatility of the mosaic electrode microstructure to different current collectors and cathode materials, we performed another two experiments. One is to expand the choice of substrate from carbon cloth to PET fabric, which is thinner, lighter, but provides the similar structure characteristics. Polyethylene terephthalate (PET) fabric is a promising candidate. As such, an ultrathin PET fabric with a thickness of 50 μm was selected and employed as the current collector after depositing the Ni layer on its surface in the same way as carbon clothes (Fig. S12). The areal density of the obtained NiPET was around 5.5 mg cm^{-2}, much smaller than NiCC. After carrying out the slurry coating process on the surface of the NiPET, a similar mosaic microstructure can also be observed on the surface of the active materials layer (Fig. 5a and 5b inset). The obtained Mosaic-S-NiPET also exhibited a high initial discharging capacity of 1140 mAh g^{-1} at 0.1 C. After 200 cycles, the Mosaic-S-NiPET cathode remained 480 mAh g^{-1} at 0.2 C. Another is the change of cathode from S to other cathode materials. Taking the $LiFePO_4$ (LFP) as the representative, the mosaic microstructure can also be obtained (Fig. 5c). The Mosaic-LFP also exhibited excellent electrochemical performance. At a high mass loading of 10 mg cm^{-2}, the Mosaic-LFP delivered a reversible capacity of 126 mAh g^{-1} after 250 cycles with an 87 % retention at 0.2 C. In addition, the Mosaic-LFP cathode also showed an outstanding rate performance (Fig. 5d and 5e). Even at 10 C, it still exhibited 90 mAh g^{-1}. After 700 cycles, a reversible capacity of 136 mAh g^{-1} can remain with a capacity retention of 99.99% per cycle at 1 C. The above results confirm the universality of the cracking-controlled slurry coating method with different fabric substrates and active materials, demonstrating its potential scalability.

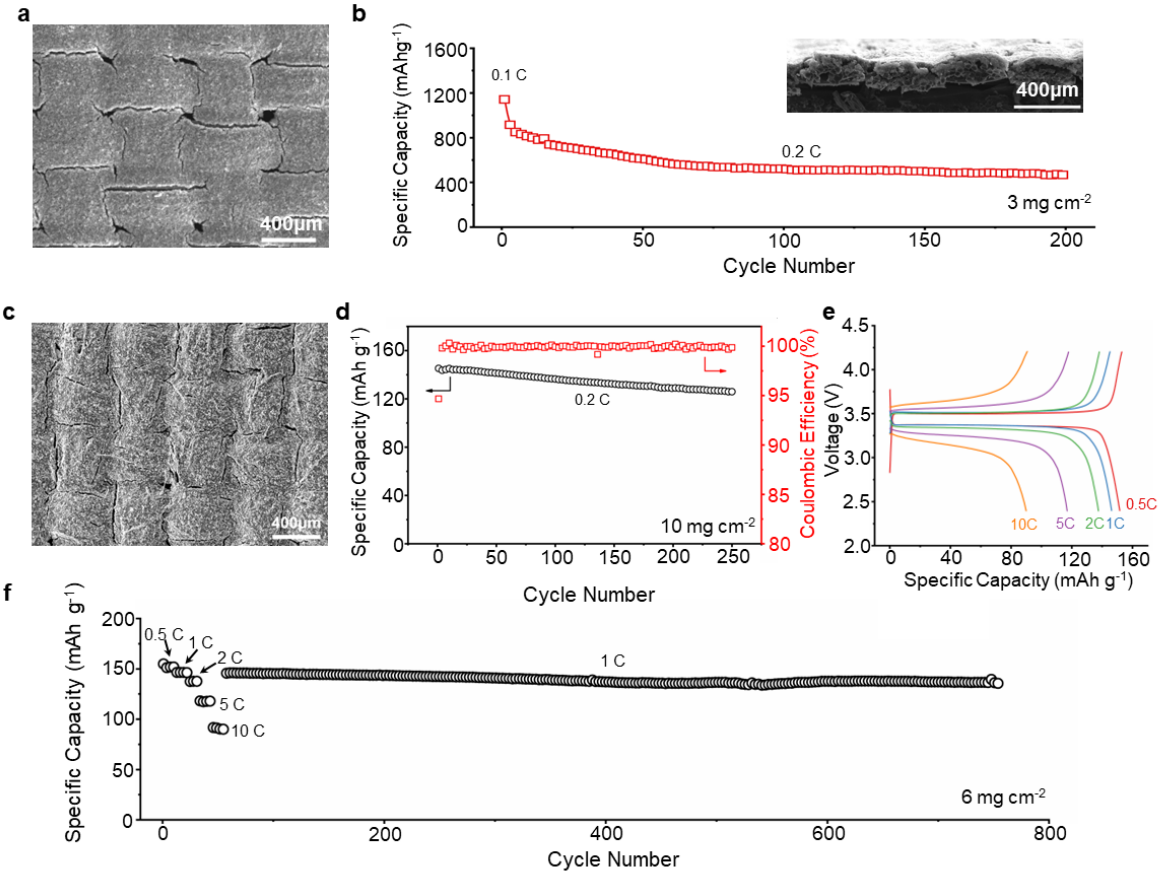

Figure 5. a) SEM image of the Mosaic-S-NiPET cathode. b) Cyclic performance of the Mosaic-S-NiPET cathode with a mass loading of 3 mg cm^{-2}. c) SEM image of the Mosaic-LFP cathode. d) Cyclic performance of the Mosaic-LFP cathode with a mass loading of 10 mg cm^{-2} at 0.2 C. e) Voltage profiles of the Mosaic-LFP cathode with a mass loading of 6 mg cm^{-2} at different rates. f) Long cycle performance of the Mosaic-LFP cathode with a mass loading of 6 mg cm^{-2}.

Conclusions

We have developed a simple and high-throughput cracking-controlled method to fabricate high-performance flexible Mosaic-S cathode. The Mosaic-S cathode possesses regular cracks, which served as the vertical channels to facilitate ionic diffusion, and provided enough space to accommodate the volume variation of the S cathode during cycling. Therefore, the fabricated Mosaic-S cathode with a high mass loading delivered a high energy density of 560

Wh kg^{-1}. The Mosaic-S cathode also exhibits outstanding mechanical stability benefiting from the pre-defined crack patterns. Incorporated with a flexible Li anode, the assembled pouch cell showed nearly 7800 bending times with a radius of 5 mm in one discharging/charging process without any voltage shift. Importantly, the fabrication process is very simple and the throughput is similar to the industrial slurry coating method. Because this method only requires a good control of the wetting and drying speed of the liquid slurry on the interlacing fabric, it is highly compatible with a wide variety of active materials for energy and environmental applications.

Experimental Section

Preparation of nickel-coated carbon clothes and nickel-coated PET: Commercially available carbon clothes (CC) were first immersed in a mixture of concentrated H_2SO_4 and HNO_3 (v/v=3:1) at 80 ℃ for 3 h. After rinsing with the deionized water several times, the treated CC dried at 80 ℃ overnight. Coating a nickel layer on the CCs is a typical polymer-assisted metal deposition process. During this process, the treated CCs were immersed into a mixture of ethanol, acetic acid, and deionized water in a volumetric ratio of 95:1:4, containing 4%, v/v [3-(methacryloyloxy)propyl]trimethoxysilane for 1h at room temperature to silanize. After rinsing several times, the silanized CC was then immersed in the 20 % [2-(methacryloyloxy)ethyl]trimethyl ammonium chloride (METAC) aqueous solution by volume, containing 2g L^{-1} potassium persulfate. The following polymerization of METAC carries out at 80 ℃ for 1 h to obtain a PMETAC layer. After washing with deionized water for several times, the PMETAC coated CC was then dipped into an $(NH_4)_2PdCl_4$ aqueous solution (5×10^{-3} M). Finally, the $[PdCl_4]^{2-}$ loaded CC with PMETAC layer was immersed into the ELD bath for 30 min. The ELD bath contained a mixed solution A and B. Solution A (pH=7.5) comprised of $NiSO_4 \cdot 6H_2O$ (80 g L^{-1}), sodium citrate (40 g L^{-1}), and lactic acid (20 g L^{-1}), and Solution B dissolved 1.5 g L^{-1} of dimethylamine borane (DMAB). The fabrication process of NiPET is

similar to that of NiCC, and the only difference is that the H_2SO_4/HNO_3 treatment process needs to be replaced by a NaOH treatment. The PET was set in a 2M NaOH solution bath for 4h. After rinsing with the deionized water several times, the treated PET dried at 60 ℃ overnight, and then proceeded with the same Ni layer coating process.

Preparation of sulfur cathodes: Sulfur powder was first grounded with acetylene black with a mass ratio of 4:1. Then the S/ACB composites were heat-treated at 155 ℃ for 12 h. Polyvinylidene difluoride and poly(styrene-co-maleic anhydride) worked as co-binders here with a mass ratio of 1:1. S/ACB, SuperP powder, and co-binder in a weight ratio of 15:3:2 were mixed and grounded for ~ 30 min in N-Methyl pyrrolidone (NMP) solution. The prepared slurry was then cast onto the Al foil and CC current collector, followed by a drying process of 45 ℃ for 2~4 h. The obtained cathodes were cut into pieces with a diameter of 12 mm with a mass loading of 2.6 mg cm^{-2} for the following electrochemical tests.

Preparation of LFP cathodes: LFP powder was grounded with acetylene black and polyvinylidene difluoride with a mass ratio of 8:1:1 for ~ 30 min in N-Methyl pyrrolidone (NMP) solution. The prepared slurry was then cast onto the CC current collector, followed by a drying process of 60 ℃ for 2~4 h. The obtained LFP cathodes were cut into pieces with a diameter of 12 mm with a mass loading of 6 and 10 mg cm^{-2} for the following electrochemical tests.

Preparation of electrodeposited lithium anode: The nickel-coated CC was cut into a certain size as the working electrode for the following electrodeposition. Separated by the PP separator, a 200 μm Li Foil and the nickel-coated CC was assembled in the commercial soft Al-plastic film pouch cell in the argon-filled glove box. The electrolyte is a mixture solution of 1,3-dioxolane (DOL) and 1,2-dimethoxyethane (DME) (*v*:*v*=1:1) containing 1M lithium

bis(trifluoromethanesulfonyl)imide (LiTFSI) with 2 % $LiNO_3$ additives. The added electrolyte in the pouch cell was about 10 μL cm^{-2}. The assembled cell was first discharged to 8 mAh cm^{-2} and charged to 3 V at a current density of 1 mA cm^{-2} for 3 cycles. Finally, the cell discharged to 8 mAh cm^{-2} at a current density of 0.5 mA cm^{-2} for the flexible battery assembly.

Assembly of the flexible full pouch cell: The prepared Mosaic-S cathode, PP separator, and the electrodeposited lithium anode were assembled in the pouch cell in the argon-filled glove box. The size of the Mosaic-S cathode is 2×3 cm^2. The mass loading of the sulfur cathode is ~ 6 mg cm^{-2}, and the electrolyte used for the full cell was also 40 μL cm^{-2}.

Characterization: The surface morphology of the sulfur electrode and lithium anode and the corresponding EDS mapping was observed by the field emission scanning electron microscopy (FESEM, TESCAN MAIA3, Brno, Czech Republic). The single-tap shear tests were performed on an Instron 5565 A tester. The sheet resistance results were obtained by a four-probe method through a Keithley 2400 sourcemeter.

Electrochemical measurements: All the 2032-typed coin cells and pouch cells were assembled in the glove box under the Argon atmosphere. When assembling the coin cell, the prepared sulfur cathode, PP separator, and 200 μm Li foil were set in turn. The amount of electrolyte used for the galvanostatic discharging/charging performance was 30 μL cm^{-2}. The cyclic and rate performance were conducted on the Neware battery testing system. The mass loading for the long cycling performance was 1.8 mg cm^{-2}. The CV, EIS, and low-tortuosity tests were performed on a CHI660e electrochemical working station. The CV results were obtained at a scan rate of 0.2 mV s^{-1} in the range of 1.6-2.8 V. The EIS spectra were done within a frequency range of 10^5-0.1 Hz. For the low tortuosity tests, The cells were first allowed to rest for at least 2 h before the low-tortuosity testing to ensure the wettability of the electrolyte. Then a current

of 10 μA was applied to the cell for 2 h before interrupting the current. Until $\frac{dU}{dt} < 0.1\ mV\ h^{-1}$, the data was finally collected. The obtained plots should follow the formula of relaxation voltage $U(t)$,[44,45]

$$U(t) = \left[\frac{i_p L}{\sigma}\right] + \left(\frac{\sigma_{el}}{\sigma}\right)\left(\frac{i_p L}{\sigma_{ion}}\right)\{1 - \left(\frac{8}{\pi^2}\right)\exp\left[\left(-\frac{t}{t^{\delta}}\right)\right]\} \quad (3)$$

Where i_p is the applied current, L is the thickness of sulfur cathodes, σ, σ_{el}, and σ_{ion} are the total, electronic and ionic conductivities, respectively, and t^{δ} is the characteristic value related to the relaxation time of the depolarization process.

Supporting Information

Supporting Information is available from the Wiley Online Library or from the author.

Acknowledgements

The authors acknowledge the financial support from the Shenzhen Municipal Science and Technology Innovation Commission (SGDX20190816232209446), Innovation and Technology Fund-Guangdong-Hong Kong Technology Cooperation Funding Scheme (GHP/047/20GD), and Science and Technology Bureau of Huangpu District (2020GH03).

Received: ((will be filled in by the editorial staff))

Revised: ((will be filled in by the editorial staff))

Published online: ((will be filled in by the editorial staff))

References

[1] Y. J. Li, S. J. Guo, *Matter* **2021**, 4, 1142.

[2] S. Dorfler, H. Althues, P. Hartel, T. Abendroth, B. Schumm, S. Kaskel, Joule **2020**, 4, 539.

[3] T. Li, X. Bai, U. Gulzar, Y.-J. Bai, C. Capiglia, W. Deng, X. F. Zhou, Z. P. Liu, Z. F. Feng, R. P. Zaccaria, *Adv. Funct. Mater.* **2019**, 29, 1901730.

[4] Z. H. Wei, Y. Q. Ren, J. Sokolowski, X. D. Zhu, G. Wu, *InfoMat* 2020, 2, 483.

[5] Y.-X. Yao, X.-Q. Zhang, B.-Q. Li, C. Yan, P.-Y. Chen, J.-Q. Huang, Q. Zhang, *InfoMat* 2020, 2, 379.

[6] Y. Gao, C. Xie, Z. J. Zheng, *Adv. Energy Mater.* **2021**, 11, 2002838.

[7] L. C. Zeng, L. Qiu, H. M. Cheng, *Energy Storage Mater.* **2019**, 23, 434.

[8] J. Chang, Q. Huang, Z. J. Zheng, *Joule* **2020**, 4, 1346.

[9] Q. H. Q. Xiao, J. L. Yang, X. D. Wang, D. R. Deng, P. Han, N. Yuan, L. Zhang, M. Feng, C.-A, Wang, R. P. Liu, *Carbon Energy* **2021**, 3, 271.

[10] T. Yang, J. Xia, Z. H. Piao, L. Yang, S. C. Zhang, Y. L. Xing, G. M. Zhou, *ACS Nano* **2021**, 15, 13901.

[11] Z. Y. Cao, B, Q, Wei, *Energy Environ. Sci.* **2013**, 6, 3183.

[12] R. C. Lu, M. Cheng, L. J. Mao, M. Zhang, H. X. Yuan, K. Amin, C. Yang, Y. L. Cheng, Y. N. Meng, Z. X. Wei, *Ecomat* **2020**, 2, e12010.

[13] K. N. Chen, J. Cao, Q. Q. Lu, Q. R. Wang, M. J. Yao, M. M. Han, Z. Q. Niu, J. Chen, *Nano Research* **2018**, 11, 1345.

[14] Z. H. Fang, Y. F. Luo, H. C. Wu, L. J. Yan, F. Zhao, Q. Q. Li, S. S. Fan, J. P. Wang, *Carbon* **2020**, 166, 183.

[15] J. R. He, Y. F. Chen, W. Q. Lv, K. C. Wen, P. J. Li, F. Qi, Z. G. Wang, W. L. Zhang, Y. R. Li, W. Qin, W. D. He, *J. Power Sources* **2016**, 327, 474.

[16] G. M. Zhou, L. Li, C. Q. Ma, S. G. Wang, Y. Shi, N. Koratkar, W. C. Ren, F. Li, H.-M. Cheng, *Nano Energy* **2015**, 11, 356.

[17] H. Tang, L. You, J. W. Liu, S. Q. Wang, P. Y. Wang, C. Q. Feng, Z. P. Guo, *ACS Appl. Mater. Interfaces* **2019**, 11, 18448.

[18] X.-W. Wu, H. Xie, Q. Deng, H.-X. Wang, H. Sheng, Y.-X. Yin, W.-X. Zhou, R.-L. Li, Y.-G. Guo, *ACS Appl. Mater. Interfaces* **2017**, 9, 1553.

[19] T.-Z. Hou, X. Chen, H.-J. Peng, J.-Q. Huang, B.-Q. Li, Q. Zhang, *Small* **2016**, 12, 3283.

[20] Y. Yao, H. Y. Wang, H. Yang, S. F. Zeng, R. Xu, F. F. Liu, P. C. Shi, Y. Z. Feng, K. Wang, W. J. Yang, X. J. Wu, W. Luo, Y. Yu, *Adv. Mater.* **2020**, 32, 1905658.

[21] F. He, J. Ye, Y. L. Cao, L. F. Xiao, H. X. Yang, X. P. Ai, *ACS Appl. Mater. Interfaces* **2017**, 9, 11626-11633.

[22] Z. X. Shi, M. Li, J. Y. Sun, Z. W. Chen, *Adv. Energy Mater.* **2021**, 11, 2100332.

[23] R. Razaq, N. N. Zhang, Y. Xin, Q. Li, J. Wang, Z. L. Zhang, *Ecomat* **2020**, 2, e12020.

[24] Y. S. Zhang, P. Zhang, S. J. Zhang, Z. Wang, N. Li, S. R. P. Silva, G. S. Shao, *InfoMat* **2021**, 3, 790.

[25] L. Ji, X. Wang, Y. F. Jia, Q. L. Hu, L. M. L. Duan, Z. B. Geng, Z. Q. Niu, W. S. Li, J. H. Liu, Y. G. Zhang, S. H. Feng, *Adv. Funct. Mater.* **2020**, 30, 1910533.

[26] D. H. Liu, C. Zhang, Z. Xu, L. Zhang, W. Lv, X. L. Zou, F. Y. Kang, L. J. Zhi, H-M. Cheng, Q.-H. Yang, *Nano Energy* **2017**, 41, 665.

[27] W. C. Ren, W. Ma, S. F. Zhang, B. T. Tang, *Chem. Eng. J.* **2018**, 341, 441.

[28] C. Dillard, S.-H. Chung, A. Singh, A. Manthiram, V. Kalva, *Mater. Today Energy* **2018**, 9, 336.

[29] J. Xia, W. X. Chen, Y. Yang, X. G. Guan, T. Yang, M. J. Xiao, S. C. Zhang, Y. L. Xing, X. Lu, G. M. Zhou, *Ecomat* **2022**, e12183.

[30] J. Chang, H. Hu, J. Shang, R. P. Fang, D. H. Shou, C. Xie, Y. Gao, Y. Yang, Q. N. Zhuang, X. Lu, Y. K. Zhang, F. Li, Z. J. Zheng, *Small* **2021**, 2105308.

[31] J. Chang, J. Shang, Y. M. Sun, L. K. Ono, D. R. Wang, Z. J. Ma, Q. Y. Huang, D. D. Chen, G. Q. Liu, Y. Cui, Y. B. Qi, Z. Z. Zheng, *Nat. Commun.* **2018**, 9, 4480.

[32] A. Kraytsberg, Y. Ein-Eli, *Adv. Energy Mater.* **2016**, 6, 1600655.

[33] D. D. Liu, Y. C. Chen, H. He, Y. Y. He, H. Liu, B. Zhang, *Prog. Chem.* **2018**, 30, 765.

[34] M. A. Pope, I. A. Aksay, *Adv. Energy Mater.* **2015**, 5, 1500124.

[35] Q. L. Zou, Y.-C. Lu, *Ecomat* **2021**, 3, e12115.

[36] W. X. Ji, H. N. Qu, X. X. Zhang, D. Zheng, D. Y. Qu, *Small Methods* **2021**, 2100518.

[37] H. Kwack, J. Lee, W. Jo, Y.-J. Kim, H. Noh, H. Chu, H.-T. Kim, *ACS Appl. Mater. Interfaces* **2019**, 11, 29849.

[38] D. P. Lv, J. M. Zheng, Q. Y. Li, X. Xie, S. Ferrara, Z. M. Nie, L. B. Mehdi, N. D. Browning, J.-G. Zhang, G. L. Graff, J. Liu, J. Xiao, *Adv. Energy Mater.* **2015**, 5, 1402290.

[39] J. W. Choi, D. Aurbach, *Nat. Rev. Mater.* **2016**, 1, 16013.

[40] S.-G. Woo, S. Yoo, S.-H, Lim, J.-S. Yu, K. Kim, J. Lee, D. G. Lee, J.-H. Kim, S.-Y. Lee, *Adv. Funct. Mater.* **2020**, 30, 1908633.

[41] T. Koshi, K.-I. Nomura, M. Yoshida, *Micromachines* **2020**, 11, 209.

[42] Y. Ko, J.-S. Kim, C. C. Vu, J. Kim, *Sensors* **2021**, 21, 2531.

[44] H.-W. Park, M.-S. Jang, J.-S. Choi, J. Pyo, C.-G. Kim, *Composite Structures* **2021**, 256, 112999.

[44] J. Xu, J. Varna, *J. Compos. Mater.* **2019**, 53, 3615.

[45] J. Xu, J. Varna, *Compos. Sci. Technol.* **2020**, 186, 107891.

[46] I. V. Thorat, D. E. Stephenson, N. A. Zacharias, K. Zaghib, J. N. Harb, D. R. Wheeler, *J. Power Sources* **2009**, 188, 592.

[47] B. Delattre, R. Amin, J. Sander, J. D. Coninck, A. P. Tomsia, Y-M. Chiang, *J. Electrochem. Soc.* **2018**, 165, A388.

[48] X. Zhang, Z. Y. Hui, S. King, L. Wang, Z. Y. Ju, J. Y. Wu, K. J. Takeuchi, A. C. Marschilok, A. C. West, E. S. Takeuchi, G. H. Yu, *Nano Lett.* **2021**, 21, 5896.

[49] M. Ebner, D. W. Chung, R. E. Garcia, V. Wood, *Adv. Energy Mater.* **2014**, 4, 1301278.

[50] M. Doyle, J. Newman, A. S. Gozdz, C. N. Schmutz, J. M. Tarascon, *J. Electrochem. Soc.* **1996**, 143, 1890.

[51] Z. F. Deng, Z. A. Zhang, Y. Q. Lai, J. Liu, J. Li, Y. X. Liu, *J. Electrochem. Soc.* **2013**, 160, A553.

We report a cracking-controlled slurry coating method to fabricate flexible mosaic-like electrode. The regular pre-formed cracks in the Mosaic-S cathode can facilitate electrolyte diffusion, provide enough space to accommodate volume expansion during cycling, and enable a strain-releasing structure to achieve outstanding electrochemical performance and flexibility of lithium-sulfur battery.

*Yufeng Luo, Lei Wang, Zhenyao Wei, Qiyao Huang, Zijian Zheng**

Cracking-controlled slurry coating of mosaic electrode for flexible and high-performance lithium-sulfur battery

ToC figure